Int. J. Heat Mass Transfer. Vol. 35, No. 12, pp. 3301–3312, 1992
Printed in Great Britain

0017–9310/92 $5.00+0.00

Adaptive finite element analysis of axisymmetric freezing

ERWIN SUTANTO,† H. TED DAVIS‡ and L. E. SCRIVEN
Department of Chemical Engineering and Materials Science, University of Minnesota, Minneapolis, MN 55455, U.S.A.

(*Received* 10 *April* 1991 *and in final form* 7 *February* 1992)

Abstract—The paper describes an adaptive finite element analysis of the transient axisymmetric freezing process. Adaptivity schemes are applied to both space and time tessellations. Error equidistribution adjusts the nodal positions and Taylor series analysis of time truncation error selects the time step. In implicit time integration, the location of the freezing front and the nodal temperatures at the next time is solved by full Newton all at once. The method appears to be accurate; in cases for which closed-form solutions are available, it agrees well with them. It also avoids the problem found in the Modified Isotherm Migration Method where the freezing front tends to retrogress when solid just forms on the outer surface cooled by convection.

1. INTRODUCTION

FREEZING processes are common in nature and technology: examples are freezing of soil, solidification of alloys, growing of single crystals from melts, and so on. It is desirable to be able to predict the rate at which the freezing front advances. Many numerical schemes have been devised to solve both transient freezing problems [1–5] and steady-state ones [6]. Some of the numerical schemes that have been developed were reviewed by Crank [7].

In this chapter, an axisymmetric freezing problem is solved by Galerkin's method with adaptive tessellation of space into time-dependent finite elements and a finite difference approximation in time. The time integration with the finite difference also includes time step adjustment. Finite element analysis with time-dependent elements has been used by Lynch and O'Neill [5] for the same freezing problem and by Miller and Miller [8] and Benner *et al.* [9] for other transient problems. The main difference between the present analysis and that by Lynch and O'Neill is that the location of the freezing front and the nodal temperatures are found all at once by Newton's iteration, instead of iterating successively for the temperatures and then the location of the freezing front. Newton's method requires deriving the entries in the Jacobian matrix; however, the method is efficient because it converges nearly quadratically provided the correct Jacobian and a good enough initial approximation are available. Newton's method also complicates the matrix computation because the Jacobian entries in the last column and in the last row deviate from banded matrix structure. However the deviation from the banded matrix structure does not raise the cost of computation by much because bordered matrix analysis, explained later in Section 4.2, suppresses the cost increase. The present analysis also includes adaptivity schemes both in space and time. The finite elements are chosen so that a certain measure of spatial truncation error is uniformly distributed. The time steps are chosen so that a Taylor series estimate of time truncation error remains less than a preset amount.

The method appears to be accurate: in cases for which closed-form solutions are available, it agrees well with them. It also avoids a problem of the Modified Isotherm Migration Method [3], namely the tendency of the first solid that forms at the outer surface of liquid cooled by convection, to re-melt, i.e. the tendency of a newly appeared freezing front to retrogress. The method has been applied recently to solving the problem of heat conduction with radiant energy input as in thawing by microwaves [10].

2. MATHEMATICAL FORMULATION

Liquid at initial temperature T_0^* well above the freezing temperature T_f^* is frozen by plunging it into coolant at temperature T_c^*. As long as the temperature of the outer surface is higher than T_f^*, a standard analytical solution of the heat conduction problem is available. When the temperature of the outer surface drops to T_f^*, a freezing front starts advancing into the sample, and the region swept by the front becomes solid, the thermal properties of which are different from the liquid's.

To simplify the computation, the following restrictions are used: solid and liquid have the same density, the solid–liquid interface is sharp and stable, and there

† Present address: ARCO Oil and Gas Company, 2300 West Plano Parkway, Plano, TX 75075, U.S.A.
‡ Author to whom correspondence should be addressed.

NOMENCLATURE

a^*	location of freezing front
Δa	difference in location of freezing front between each Newton iteration
Bi	Biot number
c^*	specific heat
C	constant
D	distance from the center of the sample to the outer surface
E	error bound in an element
h	heat transfer coefficient
J_0	Bessel function of the first kind of order 0
K^*	thermal conductivity
L^*	heat of freezing
N	total number of nodes
N_L	number of nodes in liquid
r^*	distance
R	Galerkin weighted residual
t^*	time
Δt	time increment
T^*	temperature
T_c^*	coolant temperature
T_f^*	freezing temperature
T_0^*	initial temperature
$\Delta \mathbf{T}$	difference in nodal temperature between each Newton iteration
$\Delta T_{l,\min}$	variable used as a criterion to remove nodes in liquid
$\Delta T_{s,\max}$	variable used as a criterion to add nodes in solid
x	variable in equations (17) and (18)
y	time dependent variable in equations (11) and (12).

Greek symbols

α^*	thermal diffusivity
β	dimensionless solid specific heat
ε	variable used in equations (15) and (16) to choose size of time step
ε_T	Euclidean norm of nodal temperatures of finite element and error function solutions
λ_m	eigenvalues in closed-form solutions
ξ	distance in reference element
ρ^*	density
ϕ	finite element basis function.

Subscripts

ana.	closed-form solution
BE	backward Euler solution
cor.	corrector solution
FE	forward Euler solution
i	node index in finite element
j	node index in finite element
k	element index in finite element
l	liquid
m	eigenvalue index in analytical solution
num.	finite element solution
pred.	predictor solution
s	solid
TP	trapezoidal rule solution
UFD	uncentered finite difference solution.

Superscripts

d	exponent indicating geometry of the sample
n	number of time step.

is no flow in the liquid phase. Closed-form solutions of the moving front problem are available only for a few cases; e.g. freezing a semi-infinite slab [11] and a semi-infinite wedge [12]. Otherwise Galerkin's method with suitable basis functions, finite difference approximation, or another approximation method must be used.

The governing equations are heat conduction equations

$$\frac{\partial T}{\partial t} - \frac{1}{r^d}\frac{\partial}{\partial r}\left(r^d \frac{\partial T}{\partial r}\right) = 0 \quad \text{in the liquid, and} \tag{1}$$

$$\frac{\partial T}{\partial t} - \alpha_s \frac{1}{r^d}\frac{\partial}{\partial r}\left(r^d \frac{\partial T}{\partial r}\right) = 0 \quad \text{in the solid.} \tag{2}$$

$d = 0$ corresponds to a plate; $d = 1$, to a cylinder; and $d = 2$, to a sphere.

If the center of the sample is chosen as the origin $r = 0$, the symmetry boundary condition there is

$$\frac{\partial T}{\partial r}(0, t) = 0. \tag{3}$$

If the length scale is chosen so that the outer surface is at $r = 1$, Newton's approximation of the heat transfer from the liquid to the coolant there is

$$\beta \frac{\partial T}{\partial r}(1, t) = -Bi\, T(1, t) \tag{4}$$

where β is the normalized solid conductivity and Bi is the normalized heat transfer coefficient. If $Bi \to \infty$, the temperature of the outer surface reaches the coolant temperature right after the sample is immersed in the coolant,

$$T(1, t) = 0. \tag{5}$$

At the freezing front $r = a(t)$, the temperature is, by definition, the freezing temperature T_f, and Stefan's condition, a heat balance condition, applies:

$$T(a(t), t) = T_f \tag{6}$$

$$L\frac{\mathrm{d}(a(t))}{\mathrm{d}t} = \frac{\partial T}{\partial r}(a(t)|_l, t) - \beta \frac{\partial T}{\partial r}(a(t)|_s, t). \tag{7}$$

The units of temperature difference, length, etc. in which the variables are measured are chosen to make the following dimensionless quantities:

$$T=\frac{T^*-T_c^*}{T_0^*-T_c^*},\quad r=\frac{r^*}{D},\quad a(t)=\frac{a^*(t)}{D},$$

$$t=\frac{K_l^* t^*}{\rho_l^* c_l^* D^2},\quad \alpha_s=\frac{\alpha_s^*}{\alpha_l^*},\quad Bi=\frac{hD}{K_l^*},$$

$$L=\frac{L^*}{c_l^*(T_0^*-T_c^*)},\quad \text{and}\quad \beta=\frac{K_s^*}{K_l^*}.$$

3. GALERKIN FINITE ELEMENT ANALYSIS

The shrinking of the liquid domain and the growth of the solid domain as freezing proceeds makes tessellation into a fixed set of finite elements unsuitable. In particular, fixed elements are not able to track the exact location of the freezing front, which is required to prescribe Stefan's condition accurately. Accurate thermal properties for an element that contains the freezing front and spans both liquid and solid, an unavoidable problem in fixed-grid finite element analysis, are also not known. Fixed-grid analysis of the freezing problem is suitable after reformulating the heat conduction equations in terms of enthalpy [1, 4] or after incorporating the latent heat into the heat capacity by the Dirac delta function [13]. Finite element analysis with moving and deforming elements is a convenient method to overcome the problem of tracking the freezing front. One node is placed right at the freezing front from the start of the computation. The node moves and follows the freezing front as it advances into the sample. To accommodate the movement of the node on the freezing front, the elements in both the solid and the liquid should move and deform.

The expansion of temperature in terms of N moving and deforming basis functions is

$$T=\sum_{i=1}^{N} T_i(t)\phi_i(r,t).$$

The Galerkin weighted residuals of equations (1) and (2) with N_L number of nodes in the liquid, $0<r<a(t)$, and $(N-N_L)$ number of nodes in the solid, $a(t)<r<1$, are

$$R_i\equiv\int_0^{a(t)}\left(\phi_i\frac{\partial T}{\partial t}+\frac{\partial\phi_i}{\partial r}\frac{\partial T}{\partial r}\right)r^d\,dr=0,$$

$$i=1,N_L-1 \tag{8}$$

$$R_i\equiv\int_{a(t)}^{1}\left(\phi_i\frac{\partial T}{\partial t}+\alpha_s\frac{\partial\phi_i}{\partial r}\frac{\partial T}{\partial r}\right)r^d\,dr-\alpha_s\phi_i\frac{\partial T}{\partial r}(1,t)=0,$$

$$i=N_L+1,N. \tag{9}$$

The basis function ϕ_{N_L} associated with the node at the freezing front spans both liquid and solid so that the residual weighted by this function is

$$R_{N_L}=\int_0^{a(t)}\phi_{N_L}\frac{\partial T}{\partial t}r^d\,dr+\int_0^{a(t)}\frac{\partial\phi_{N_L}}{\partial r}\frac{\partial T}{\partial r}r^d\,dr$$
$$+\frac{\beta}{\alpha_s}\int_{a(t)}^{1}\phi_{N_L}\frac{\partial T}{\partial t}r^d\,dr+\beta\int_{a(t)}^{1}\frac{\partial\phi_{N_L}}{\partial r}\frac{\partial T}{\partial r}r^d\,dr$$
$$-\Bigg(\underbrace{\frac{\partial T}{\partial r}(a(t)|_l,t)-\beta\frac{\partial T}{\partial r}(a(t)|_s,t)}_{L\frac{d(a(t))}{dt}}\Bigg)a^d(t)=0. \tag{10}$$

The treatment of the heat balance at the moving interface using equation (10) has also been used by Ettouney and Brown [6] in their Isotherm Method and by Lynch and Sullivan [14]. Lynch and Sullivan [14] indicated that the computations using equation (10) as the heat balance at the moving interface led to a more accurate solution than those of equation (7).

Because numerical discretization of nodal temperatures in time by finite difference requires total time derivative, convected time derivatives of dT_i/dt and dr_i/dt are used to compute the partial time derivative of temperature in the residuals [15]

$$\frac{\partial T}{\partial t}=\sum_{i=1}^{N}\frac{dT_i(t)}{dt}\phi_i(r,t)$$
$$-\sum_{i=1}^{N}T_i(t)\frac{\partial\phi_i(r,t)}{\partial r}\sum_{j=1}^{N}\frac{dr_j(t)}{dt}\phi_j(\xi).$$

4. NUMERICAL STRATEGY

Figure 1 shows how equations (8), (9) and (10) along with their appropriate initial condition and boundary conditions were solved. In the examples presented in this paper, the computation always started from an initial temperature profile provided by a closed-form solution. At the start of the computation, the starting positions of nodes are adjusted in order to approximately equidistribute the error of the temperature profile among the elements. The error within each element is not exactly known; however, it can be estimated. The error estimation for each element, discussed in Section 4.1, depends on the size of the element and the spatial derivative of the temperature profile within the element. The temperature profile and the location of the freezing front at the next time step are determined by a predictor–corrector time integration scheme with a first-order accurate backward–forward Euler or a second-order accurate uncentered finite difference and trapezoidal rule. The uncentered finite difference applied to the total time derivatives is

$$\frac{dy}{dt}(t^n)=\frac{y_{UFD}(t^{n+1})-\left(\frac{\Delta t^n}{\Delta t^{n-1}}\right)^2 y(t^{n-1})-\left(1-\left(\frac{\Delta t^n}{\Delta t^{n-1}}\right)^2\right)y(t^n)}{\left(\frac{\Delta t^n}{\Delta t^{n-1}}\right)(\Delta t^n+\Delta t^{n-1})} \tag{11}$$

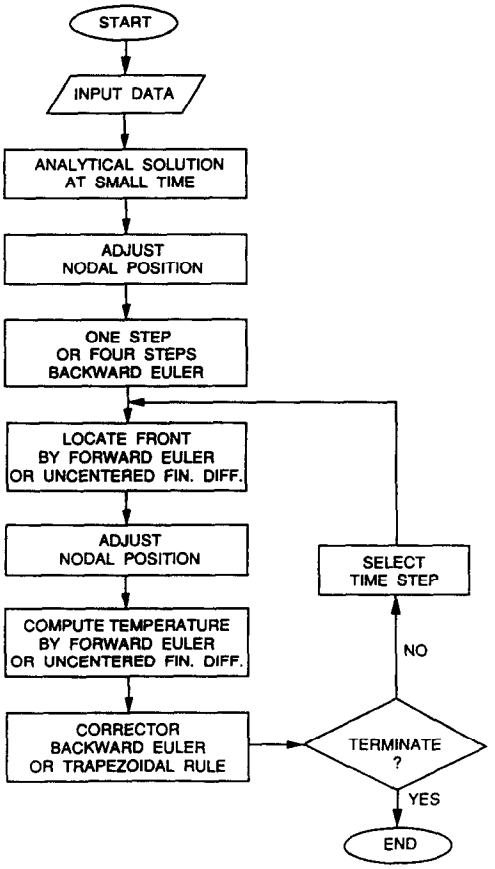

FIG. 1. Flowchart of computation.

whereas the trapezoidal rule is

$$y_{TP}(t^{n+1}) = y(t^n) + \frac{\Delta t^n}{2}\left(\frac{dy}{dt}(t^n) + \frac{dy}{dt}(t^{n+1})\right). \quad (12)$$

When Bi is finite, the numerical schemes are started after the temperature of the outer surface reaches the freezing temperature. At the first time step, explicit time integrations or trapezoidal rule of equation (9) cannot be formulated because the solid domain does not exist at the previous time. However, this is not a problem for the backward Euler method, because the method needs only liquid and solid domains at the next time; it does not require a solid domain at the previous time. Because of this problem, the backward Euler is always used to start the computation; in fact, in a second-order accurate method, the time integrations for the first four time steps are backward Euler.

4.1. *Error equidistribution*

The idea behind the error equidistribution method, as hinted by its name, is to adjust the nodal positions or the element sizes so that the error of the finite element analysis is nearly equally distributed among the elements. In a one-dimensional problem, the method tends to cluster elements in a part of the domain whose temperature profile has a high curvature and a steep gradient. Although the method does not account for the error caused by nonuniform grid spacing, which can be significant [16], it has been proved effective for solving a one-dimensional problem with steep gradients or moving shocks [9, 17].

The error equidistribution strategy used in this computation follows the continuation-adaptive method described in Benner *et al.* [9]. The difference is that the elements used here are quadratic, and an error bound for such element is [18]

$$E_k \leqslant C(\Delta r_k)^2 \int_{r_{k-1}}^{r_k} \left|\frac{\partial^3 T}{\partial r^3}\right| dr \quad (13)$$

where

$$\int_{r_{k-1}}^{r_k} \left|\frac{\partial^3 T}{\partial r^3}\right| dr = 0.5\left\{\left|\left(\frac{\partial^2 T}{\partial r^2}\right)_{k+1} - \left(\frac{\partial^2 T}{\partial r^2}\right)_k\right| + \left|\left(\frac{\partial^2 T}{\partial r^2}\right)_k - \left(\frac{\partial^2 T}{\partial r^2}\right)_{k-1}\right|\right\}.$$

As the computation progresses, nodal positions are updated at every time step according to the error equidistribution after the evaluation of $a(t^{n+1})$ in the predictor time integration. The nodal positions at the next time computed by the corrector time integration are slightly shifted from those computed by the predictor time integration. The shift of the nodal position is proportional to the shift of the front so that nodal entanglements are avoided.

In the liquid,

$$(r_i^{n+1})_{\text{cor.}} = (r_i^{n+1})_{\text{pred.}} \frac{(a^{n+1})_{\text{cor.}}}{(a^{n+1})_{\text{pred.}}}.$$

In the solid,

$$(r_i^{n+1})_{\text{cor.}} = (a^{n+1})_{\text{cor.}} + \frac{(1-a^{n+1})_{\text{cor.}}}{(1-a^{n+1})_{\text{pred.}}}(r_i^{n+1} - a^{n+1})_{\text{pred.}}.$$

4.2. *Bordered matrix analysis*

In the predictor time integration, the problem is linear. The time integration starts with determining the location of the freezing front by equation (7). The temperature profile at the end of the next time increment is then computed through equations (6), (8), (9) and the appropriate boundary conditions.

In the corrector time integration, the problem is nonlinear because the domains of the integration in equations (8), (9) and (10) are the solid and liquid domains at the next time, which are unknown. A rapid and efficient method to solve a system of nonlinear equations is the Newton iteration. For every iteration, the method solves a set of algebraic equations

$$\begin{pmatrix} \mathbf{A} & \mathbf{b} \\ \mathbf{c}^T & d \end{pmatrix}\begin{pmatrix} \Delta \mathbf{T}^{n+1} \\ \Delta a^{n+1} \end{pmatrix} = \begin{pmatrix} \mathbf{R} \\ R_{N_t} \end{pmatrix} \quad (14)$$

where

$$\mathbf{A} = \begin{bmatrix} \left(\frac{\partial R_i}{\partial T_j^{n+1}}\right)_l & & 0 \\ \cdots\cdots & \cdots\cdots & \cdots\cdots \\ 0\cdots & 1 & \cdots 0 \\ \cdots\cdots & \cdots\cdots & \cdots\cdots \\ 0 & & \left(\frac{\partial R_i}{\partial T_j^{n+1}}\right)_s \end{bmatrix},$$

$$\mathbf{b} = \begin{bmatrix} \left(\frac{\partial R_i}{\partial a^{n+1}}\right)_l \\ \cdots\cdots \\ 0 \\ \cdots\cdots \\ \left(\frac{\partial R_i}{\partial a^{n+1}}\right)_s \end{bmatrix}, \quad \mathbf{R} = \begin{bmatrix} (R_i)_l \\ \cdots\cdots \\ 0 \\ \cdots\cdots \\ (R_i)_s \end{bmatrix},$$

$$\mathbf{c}^{\mathrm{T}} = \left(\frac{\partial R_{N_L}}{\partial T_j^{n+1}}\right), \quad \text{and} \quad d = \left(\frac{\partial R_{N_L}}{\partial a^{n+1}}\right).$$

$\Delta\mathbf{T}^{n+1}$ and Δa^{n+1} in equation (14) are the difference in the nodal temperature and the location of the freezing front between each iteration. The iteration is stopped when the Euclidean norm

$$\|\Delta\mathbf{T}^{n+1}\|_2 + \|\Delta a^{n+1}\|_2 \leqslant 10^{-6}.$$

Except for the first time step, convergence with the above criterion is achieved in three or less iterations.

The matrix in equation (14) is known as a bordered matrix [19]. Because the matrix $\mathbf{A}$ is banded and its LU-decomposition can be computed cheaply, the simultaneous algebraic equations with the bordered matrix in equation (14) can be computed efficiently through

$$\Delta a^{n+1} = \frac{1}{d - \mathbf{c}^{\mathrm{T}}\mathbf{A}^{-1}\mathbf{b}}(R_{N_L} - \mathbf{c}^{\mathrm{T}}\mathbf{A}^{-1}\mathbf{R})$$

$$\Delta\mathbf{T}^{n+1} = \mathbf{A}^{-1}\mathbf{R} - \Delta a^{n+1}\mathbf{A}^{-1}\mathbf{b}.$$

4.3. *Time step selection*

In the computation, the step size taken for the next time integration is adjusted according to the Taylor series analysis of the time truncation error first suggested by Gresho *et al.* [20]. Following their error analysis, the step size taken for the next time of first-order time integration, which is computed by backward and forward Euler, is

$$\Delta t^{n+1} = \Delta t^n \left[\frac{2\varepsilon}{(\|(\mathbf{T}^{n+1})_{FE} - (\mathbf{T}^{n+1})_{BE}\|_2 + \|(a^{n+1})_{FE} - (a^{n+1})_{BE}\|_2)} \right]^{1/2}. \tag{15}$$

For second-order accurate time integration, which is computed by uncentered finite difference and trapezoidal rule, the step size for the next time is

$$\Delta t^{n+1} = \Delta t^n \left[\frac{\varepsilon\left(2\frac{\Delta t^{n-1}}{\Delta t^n} + 3\right)}{(\|(\mathbf{T}^{n+1})_{UFD} - (\mathbf{T}^{n+1})_{TP}\|_2 + \|(a^{n+1})_{UFD} - (a^{n+1})_{TP}\|_2)} \right]^{1/3} \tag{16}$$

where ε is the expected accuracy from the numerical analysis.

Because the step size in the next time in first-order time integration depends on ε to the power of 1/2 and in second-order time integration it depends on ε to the power of 1/3, the number of steps required to perform the computation at large ε is fewer in the first-order than in the second-order. However, for small values of ε, when high computational accuracy is sought, the number of steps is less in the second-order than in the first-order.

5. RESULTS AND DISCUSSION

This section discusses the examples of two different physical situations; first, freezing with infinite *Bi* and second, freezing with finite *Bi*. In the first case, a closed-form solution is available and so the robustness of the finite element computation can be evaluated. In the second case, a closed-form solution is not available. However, it is expected that the finite element computation in the second case is as accurate as the computation in the first case because the governing equations for both cases are the same, except for the boundary condition at $r = 1$.

5.1. *Freezing an infinitely wide plate of water when the Biot number is infinite*

The analytical solution of freezing with infinite *Bi* is available only for a semi-infinite slab; however the solution is also valid for a slab with finite thickness (a plate) as long as the temperature in the middle of the plate does not drop from its initial temperature. The solution [7, 11] is:

in the liquid,

$$T(r,t) = 1 + \frac{(T_f - 1)}{\operatorname{erfc}(x/2)} \operatorname{erfc}\left(\frac{1-r}{2\sqrt{t}}\right); \tag{17}$$

in the solid,

$$T(r,t) = \frac{T_f}{\operatorname{erf}\left(\frac{x}{2\sqrt{\alpha_s}}\right)} \operatorname{erf}\left(\frac{1-r}{2\sqrt{(\alpha_s t)}}\right). \tag{18}$$

The position of the advancing front is

$$a(t) = 1 - xt^{1/2}$$

where x is the solution of

$$F(x) = \frac{\beta T_f \mathrm{e}^{-x^2/(4\alpha_s)}}{\sqrt{(\alpha_s)}\operatorname{erf}\left(\frac{x}{2\sqrt{(\alpha_s)}}\right)} + \frac{(T_f - 1)\mathrm{e}^{-x^2/4}}{\operatorname{erfc}(x/2)} + \tfrac{1}{2}\sqrt{(\pi)}Lx = 0.$$

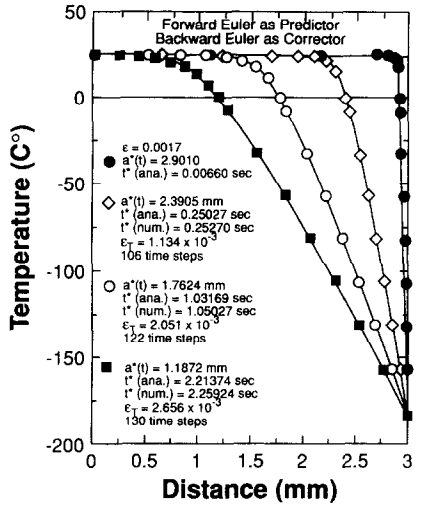

FIG. 2. Comparison of closed-form and finite element solutions of freezing an infinitely wide plate of water when Biot number is infinite. First-order time integration scheme.

Figures 2 and 3 demonstrate the performance of the finite element analysis of first- and second-order time integration. The figures show the temperature profile after the temperature of the outer surface of an infinitely wide and 6 mm thick plate of water, initially at 25°C, is suddenly dropped to −183°C. The finite element computation starts from the temperature profile obtained from the error function solution when the freezing front advances 0.099 mm into the sample. Dimensionless variables, which incorporate the thermal properties of water and ice, used in the computation are $\alpha_s = 8.43$, $\beta = 4$, $T_f = 0.8798$, $L = -0.3816$ and $t = 1.51574 \times 10^{-2} t^*$. The problem is a good example for comparing the finite element solution against the error function solution because

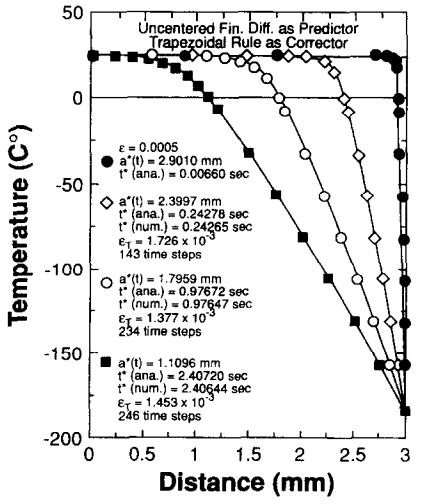

FIG. 3. Comparison of closed-form and finite element solutions of freezing an infinitely wide plate of water when Biot number is infinite. Second-order time integration.

the temperature in the middle of the sample hardly drops although 60% of the water has been frozen.

The finite element solutions shown in the figures were computed with eight quadratic elements in the liquid and eight quadratic elements in the solid. The markers on the curves in the figures are the temperature at every other node in the finite element solution, whereas the solid lines are the temperature profiles computed from the error function solution. The figures show that error equidistribution automatically adjusts the size and location of adaptive elements to resolve domains which are highly curved and/or have a steep gradient, especially at the initial temperature profile. It also puts small elements in the computation domains next to the freezing front; the small elements provide better accuracy in computing Stefan's condition. The adaptive scheme also follows the evolution of the temperature profile as the computation progresses; it stretches the adaptive elements around the steep gradient as the gradient flattens.

The time stepping procedures automatically select small step sizes, of the order of 10^{-5}, when the freezing front just advances into the sample. The procedures select larger step sizes only after the freezing front advances deep into the sample. The largest step size can attain a step size 3–4 orders of magnitude larger than the smallest step size. The same circumstances are also observed in computation with finite *Bi*.

Figures 2 and 3 illustrate the comparison of the temperature profiles obtained by the finite element solution to those obtained by the error function solution when the freezing fronts in both schemes reach the same location. Comparison in this manner is justified because the temperature in the solid and in the liquid, which are separated by the sharp freezing front, are governed by different heat conduction equations. Visual examinations of curves in the two figures indicate that the temperature profile in the finite element solution agrees well with those computed from equations (15) and (16) in terms of the error function. The good agreement is supported by the small Euclidean norms

$$\varepsilon_T = \left[\sum_{i=1}^{N} \left(\frac{(T_i)_{\text{num.}} - (T_i)_{\text{ana.}}}{(T_i)_{\text{ana.}}} \right)^2 \right]^{1/2}.$$

Surprisingly, sometimes the agreement improves as the computation progresses. Apparently, comparison of the error function and the finite element solutions at different times accidentally reduces the numerical error.

Unfortunately, the accuracy of the finite element solution of the temperature profile in space tessellation is not always accompanied by an accuracy in time integration, especially for first-order time integration. In the first-order time integration, the arrival time of the freezing front is consistently higher than the arrival time computed through the analytical solution. The disagreement worsens as the computation progresses. The following Taylor series analysis of the time truncation error for backward Euler explains the

disagreement. For each time step in the time integration, the error is [21]

$$(a^{n+1})_{BE}-(a^{n+1})_{ana.}=\frac{(\Delta t^n)^2}{2}\frac{d^2a(t)}{dt^2}+O((\Delta t^n)^3)$$
$$=\tfrac{1}{8}xt^{-3/2}(\Delta t^n)^2+O((\Delta t^n)^3)>0.$$

In the second-order time integration, the arrival time is consistently lower than the time computed analytically. Taylor series analysis of the trapezoidal rule explains the disagreement:

$$(a^{n+1})_{TP}-(a^{n+1})_{ana.}=\frac{(\Delta t^n)^3}{12}\frac{d^3a(t)}{dt^3}+O((\Delta t^n)^4)$$
$$=-\tfrac{3}{96}xt^{-5/2}(\Delta t^n)^3+O((\Delta t^n)^4)<0.$$

With eight elements in the liquid and eight in the solid, the highest attainable accuracy of first-order time integration is achieved at chosen $\varepsilon = 0.0017$: see Fig. 2. Further improvement by choosing a smaller ε, i.e. $\varepsilon < 0.0016$, is not possible because the time selection scheme selects a smaller and smaller step size and finally the program execution quits because the step size becomes smaller than the machine accuracy. Additional elements in the space tessellation are required to perform the computation at $\varepsilon < 0.0016$.

With eight elements in the liquid and eight in the solid, the highest attainable accuracy in the second-order time integration is achieved at $\varepsilon = 0.0005$: see Fig. 3. At the end of the computation, the numerical arrival time of the freezing front is accurate to within 0.03%, which is more than satisfactory. A lower ε, i.e. $\varepsilon < 0.0004$, causes the scheme to select a smaller and smaller step size. Because of the superiority of the second-order time integration, the rest of the examples presented in this paper, except where stated otherwise, were calculated with second-order time integration and $\varepsilon = 0.0005$.

5.2. *Freezing an infinitely wide plate when the Biot number is finite*

Figure 4 shows the temperature profiles during freezing of an infinitely wide 6 mm thick plate with

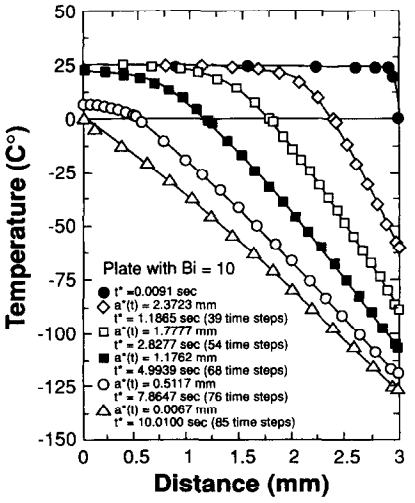

FIG. 4. Temperature profile of freezing an infinitely wide plate of water in cryogen at −183°C.

$Bi = 10$, a Biot number at the upper end of the range for freezing a thin plate in most practical situations. The finite element computation starts from the temperature profile calculated from the closed-form solution for the moment the outer surface just reaches freezing temperature. The closed-form solution is [11]

$$T(r,t)=\sum_{m=1}^{\infty}\frac{2\,Bi\sin(\lambda_m)}{\lambda_m\,Bi+\lambda_m\sin^2(\lambda_m)}\cos(\lambda_m r)\,e^{-\lambda_m^2 t} \quad (19)$$

where the eigenvalues λ_m are computed from

$$Bi=\lambda_m\tan(\lambda_m).$$

The markers on the curves in Fig. 4 are the temperature at every other node. The curves show that the error equidistribution automatically puts a small element next to the outer surface. The small element is required to represent accurately Newton's law of cooling on the surface.

Initially, the liquid domain has eight quadratic elements and the solid domain has one. As the computation progresses, some nodes in the liquid domain are removed as the domain shrinks and additional nodes are added to the solid domain as that domain swells. The removal and addition of nodes is controlled by the following criteria. Every other node in the liquid is removed if

$$\frac{2(T(0,t)-T_f)}{(N_L-1)}<\Delta T_{l,min}.$$

Additional nodes are inserted between every other nodes in the solid if

$$\frac{2(T_f-T(1,t))}{N-N_L}>\Delta T_{s,max}.$$

Removal of nodes might save some computation time, because it reduces the number of algebraic equations. However, early node removal causes a numerical problem (explained in Section 5.4) which instead probably costs more computation time. For all computations presented in this paper, except where stated otherwise, we chose $\Delta T_{l,min} = 3\times10^{-5}$ and $\Delta T_{s,max} = 5\times10^{-2}$.

5.3. *Dynamics of the propagation of freezing front*

Figure 5 illustrates the dynamics of the propagation of the freezing front both when the Biot number is finite and when it is infinite. The location of the front and the front speed are plotted against time. In the case of finite *Bi*, the front speed is computed from equation (7). Temperature profiles in the quadratic elements on both sides of the freezing front are used to compute the thermal gradients. In the case of infinite *Bi*, the existing closed-form solution provides the front speed.

The figure shows that the dynamics of front propagation when the Biot number is finite are different from those when the Biot number is infinite. This indicates that calculation with infinite *Bi* is not a good

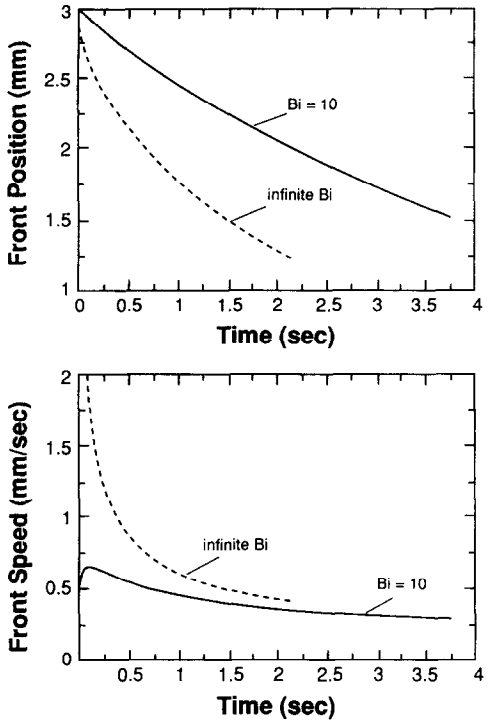

FIG. 5. History of the freezing front position and the freezing front speed in a liquid plate frozen when Biot number is infinite and when it is finite.

thermal resistance between the outer surface and the coolant cannot be neglected. The differences in the dynamic behavior are most apparent at the onset of front propagation. The front computed with infinite *Bi* advances several times deeper than the front computed with finite *Bi*. Moreover, the front speeds behave differently.

In freezing with infinite *Bi*, the front starts advancing into the plate at infinite speed. The following analysis of equation (7) explains the infinite speed. In the case of infinite *Bi*, the temperature at the outer surface abruptly plunges to the coolant temperature causing an infinite thermal gradient in the solid domain. The thermal gradient in the solid is infinite because the two opposing surfaces, i.e. the liquid–solid interface and the solid–coolant interface that sandwich the vanishingly thin solid domain, are at different temperatures. As indicated by equation (7), the infinite temperature gradient in the solid causes infinite front speed.

In the freezing process with finite *Bi*, the front starts advancing into the plate with vanishing speed because the solid temperature at the outer surface falls gradually. The heat balance in equation (7) suggests that the freezing front will not advance into the plate unless the thermal gradient in the solid is steep enough to move the front. Once the front penetrates into the plate, its advance accelerates because the solid temperature at the outer surface rapidly declines; the declining temperature steepens the thermal gradient in the thin solid domain. As the solid thickens, the thermal gradient on the solid side of the freezing front lessens and, as a consequence, the front speed falls. The thicker and cooler solid also slows down the rate of heat transfer from the freezing front to the outer surface. The rate of heat released from the outer surface to the coolant also falls because the outer surface cools.

The vanishing speed at the onset of the freezing process causes excessive numerical error if the calculation starts with introducing an artificial thin solid domain on the outer surface [3], especially if the thermal gradient in the artificial solid is too low. The introduction of a thin solid domain steepens the thermal gradient in the liquid next to the freezing front if the temperature profile in the liquid is not adjusted. The steepening thermal gradient in the liquid along with the low thermal gradient in the solid moves the freezing front outward instead of inward.

The present computation method does not require introduction of an artificial solid on the outer surface to start the calculation, because backward Euler automatically delivers a solid domain along with appropriate thermal gradients on both sides of the freezing front. The proper thermal gradients eliminate the problem of the freezing front moving outward.

5.4. *Freezing water-bearing sandstone in cryogen*

This section describes the dynamics of the freezing process in three different simple geometries: plate, cylinder, and sphere. As an example, temperatures are calculated using effective thermal properties of water-bearing sandstone. The properties of water-bearing sandstone are used because the original motivation of this work was to estimate the time required to freeze a 25°C cylindrical water-bearing sandstone, 10 mm long and 6 mm diameter in nitrogen slush at −183°C. Fast-freezing of liquid-bearing sandstone is required before it can be examined under a scanning electron microscope [22]. In dimensionless variables, the numerical values are as follow: $\alpha_s = 1.27$, $\beta = 1.07$, $T_f = 0.8798$, $L = -0.1143$, and $t = 0.181618\ t^*$. In all geometries, the distance from the outer surface to the center of the sample is 3 mm.

The computation was started from the temperature profile obtained from a closed-form solution when the outer surface just reaches freezing temperature. The closed-form solution for a plate is given by equation (19). In terms of Bessel functions, the solution for a cylinder is [11]

$$T(r,t) = \sum_{m=1}^{\infty} \frac{2\,Bi\,J_0(\lambda_m r)}{(\lambda_m^2 + Bi^2)J_0(\lambda_m)} e^{-\lambda_m^2 t} \qquad (20)$$

where the eigenvalues λ_m are computed from

$$\lambda_m J_0'(\lambda_m) + Bi\,J_0(\lambda_m) = 0.$$

In terms of sine functions, the solution for a sphere is [11]

$$T(r,t) = \sum_{m=1}^{\infty} \frac{2\,Bi \sin(\lambda_m)}{\lambda_m^2 + (Bi-1)\sin^2(\lambda_m)} \frac{\sin(\lambda_m r)}{r} e^{-\lambda_m^2 t} \tag{21}$$

where the eigenvalues λ_m are computed from

$$Bi = 1 - \lambda_m \cot(\lambda_m).$$

The time integrations for the first four time steps are computed by the backward Euler method with constant step size $\Delta t = 5 \times 10^{-5}$. After the first four time steps, the front penetrates about 5×10^{-4} mm deep into the sample. From this step onward, the automatic second-order time-stepping procedure described in Section 4.3 computes the time integration.

Figure 6 shows the temperature profile of the freezing process in a plate with $Bi = 1$ and $\varepsilon = 0.0006$. Markers on the curve in the figure are the temperatures at every other node. At first the temperature profiles in the solid phase are close to straight lines. The profile becomes slightly concave downward only after the advancing front gets close to the middle of the plate. In the liquid phase, at first the temperature profile is highly curved and gradually it flattens as the freezing front advances deeper into the sample. As the freezing front gets close to the middle of the sample, the profile becomes flat.

In the computation shown in Fig. 6, $\Delta T_{l,\min} = 0.01$ was used as a criterion to remove some nodes in the liquid phase. At this high $\Delta T_{l,\min}$, the number of elements in the liquid falls from 8 to 4 at $a^*(t) \approx 1.65$ mm, from 4 to 2 at $a^*(t) \approx 1.28$ mm, and from 2 to 1 at $a^*(t) \approx 0.96$ mm.

Figures 7 and 8 show the temperature profiles of the freezing process in a cylinder and in a sphere. Markers on the curves in the figures are the temperatures at every other node. In the computations, a small element is put next to the center of the sample because otherwise the temperature at the center oscillates and drops significantly at the onset of the computation with trapezoidal rule. The excessive numerical error causes difficulties to advance the freezing front at the start of the computation; sometimes the front moves outward. The problem does not show up in the case of freezing a plate though. Apparently the temperature oscillations in area close to the center of a cylinder and a sphere are more sensitive than those in the middle of a plate. The temperature oscillations might be caused by the added r and r^2 terms in the Galerkin, or weak, formulations of cylindrical and spherical domains.

The temperature profiles of the freezing process in a cylinder and in a sphere are slightly different from those in a plate. At first the temperature profiles in the solid phase are close to a straight line. The profile gradually curves concave downward as the freezing front advances deeper into the sample. As the freezing

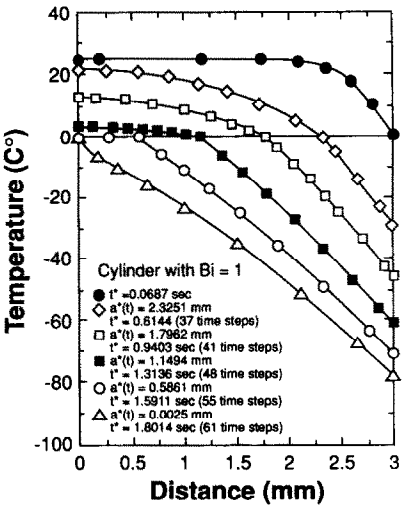

FIG. 7. Temperature profile of freezing an infinitely long cylinder of water-bearing sandstone in cryogen at −183°C with $Bi = 1$.

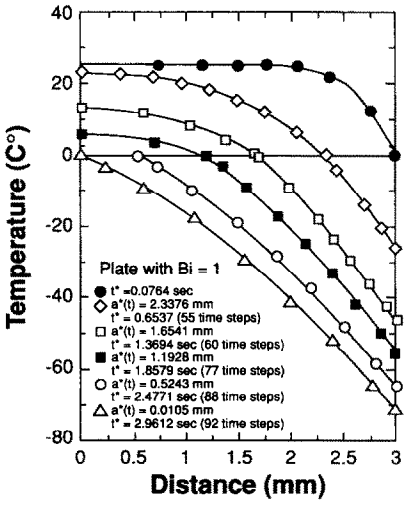

FIG. 6. Temperature profile of freezing an infinitely wide plate of water-bearing sandstone in cryogen at −183°C with $Bi = 1$. Early node removal (see text).

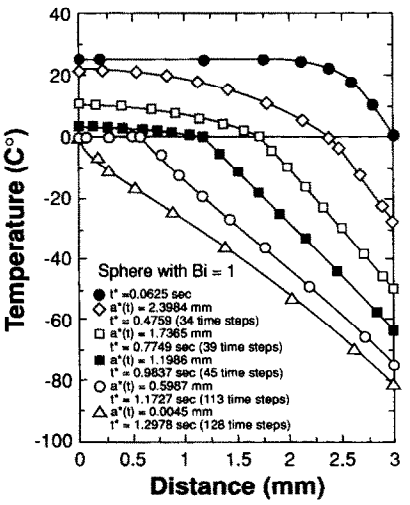

FIG. 8. Temperature profile of freezing a sphere of water-bearing sandstone in cryogen at −183°C with $Bi = 1$.

front gets close to the center of the sample, the profile inflects; it is concave upward in the solid domain close to the front and is concave downward in the solid domain far from the front. The inflection provides a high thermal gradient in the solid phase next to the freezing front and speeds up the movement of the advancing freezing front. The temperature profiles in the liquid are similar to those in the plate except the profiles in a cylinder and a sphere flatten at a faster rate.

Figure 9 shows that the dynamics of the propagation of freezing fronts in a plate, in a cylinder, and in a sphere are different. In the case of freezing a plate of liquid, the front at first accelerates rapidly; however, after the front advances to a certain thickness, the front speed hovers at about 1 mm s^{-1}. The front accelerates for the second time although the acceleration is small. The reduction of the thermal gradient in the liquid phase to a vanishing gradient causes the small acceleration. In the case of freezing a cylinder of liquid, the front also accelerates rapidly at the beginning of the process, the front speed then hovers at about 1.5 mm s^{-1}, and finally the front accelerates rapidly for the second time as it gets close to the center of the cylinder. The dynamics of the freezing front in a sphere are similar to those of freezing a cylinder, except the front speed never hovers: it always increases.

In a cylinder and a sphere, the liquid mass solidified as the front passes a certain distance lessens as the freezing front gets close to the center of the sample. In a cylinder, the liquid mass solidified by the front moving at a certain distance is proportional to $a(t)$ and, in a sphere, it is proportional to $a(t)^2$. Reduction of the liquid mass solidified causes the second front acceleration in the case of freezing a cylinder. In the case of freezing in a sphere the reduction is more significant and so the front speed never decreases; it always increases. In a plate, the liquid mass solidified by the same moving distance remains constant during the whole process.

The dotted wiggles pointed by arrows in Fig. 9 are the front speed computed by equation (7) with $\Delta T_{l,\min} = 0.01$. The wiggles are easy to identify if the axis of the front speed in Fig. 9 is stretched: see Fig. 10. Figure 10 shows three occurrences of wiggles. The first corresponds to the first reduction of elements in the liquid from 8 to 4, the second to the second removal of nodes, and the third to the third removal of nodes. The inset of Fig. 10 magnifies further the first occurrence of the wiggles. Apparently, the node removal, especially the removal of the node next to the front, disrupts the accuracy of the computation of Stefan's condition. If the computation is repeated with $\Delta T_{l,\min} = 0.001$, where the first removal of nodes is delayed and occurs when $a(t) \approx 0.9$ mm, the wiggles disappear (solid line in the lower plots in Fig. 9 and in Fig. 10 and also solid line in the inset of Fig. 10).

However, the occurrence of wiggles does not reduce the accuracy of the arrival time of the freezing front; the dotted line and the solid line in the history of the front position fall on top of each other (top of Fig. 9). The accuracies of the arrival time of the freezing front and the temperature profile are preserved because in the finite element analysis the front movement is evaluated through the trapezoidal rule, namely equation (10). The front speed computed by this method also produces wiggles: compare the dashed line in Fig. 10 and the dashed line in the inset of the figure. However, the amplitudes of the wiggles are

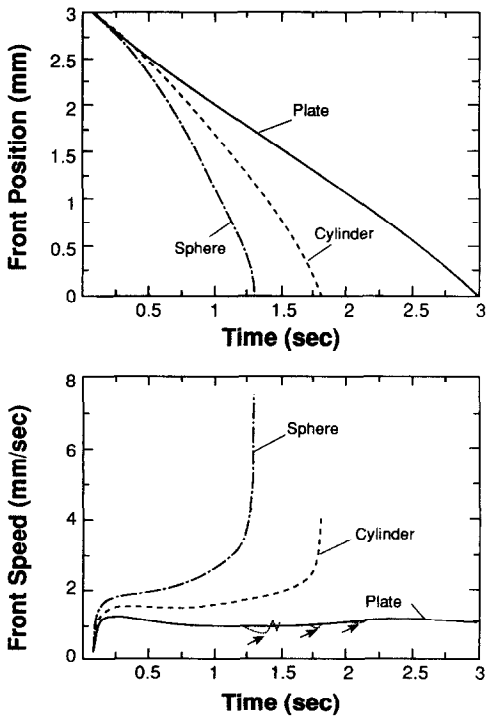

FIG. 9. History of the freezing front position and the freezing front speed in a plate, a cylinder, and a sphere.

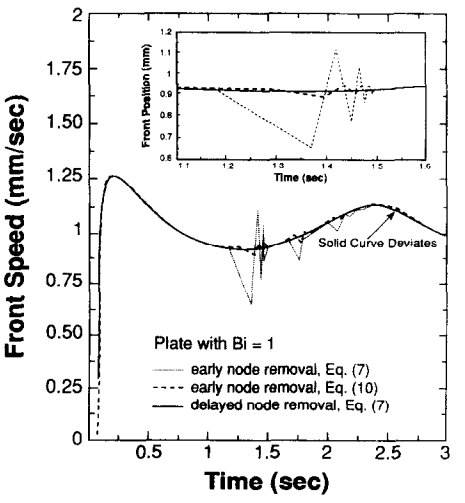

FIG. 10. The effect of early node removal on the history of the freezing front speed in a plate.

several times smaller than the dotted wiggles. The computation with the trapezoidal rule is accurate; it agrees with the computation with delayed nodal removal even after the occurrence of wiggles, notably after the decay of the third wiggles where the dotted line deviates from the solid and the dashed lines. An arrow in Fig. 10 points out an area where the solid line deviates from the dashed line. The deviation is not caused by numerical artifacts. It is caused by a lack of data points for the solid line in the region because the computation with delayed node removal takes a big time step. In the region to the lower right of the arrow the three lines agree very well.

The versatility of the automatic time-stepping procedure is the second reason that numerical accuracy is maintained. When the first wiggle occurs, the time-stepping procedure automatically selects a smaller and smaller time step until the solutions of the predictor time integration agree with those of the corrector time integration (inset of Fig. 10). From $t^* = 1.1$ s to $t^* = 1.6$ s, the computation with early node removal takes 13 time steps, whereas the computation with delayed node removal, which is free of wiggles, takes only 4 time steps. The time step taken right after the occurrence of the wiggles gets smaller and smaller because of the widening disagreement between the solution provided by uncentered finite difference, where the front movement is computed from equation (7), and the solution provided by trapezoidal rule, where the front movement is computed from equation (10).

Because early node removal causes wiggles and costs more time steps, it is better to remove nodes in the liquid at later times. Probably a better node removal scheme is one that can remove some nodes in the liquid phase except the two nodes that are closest to the freezing front. Such a removal scheme would preserve the liquid thermal gradient next to the freezing front computed by quadratic elements so that the numerical approximation of Stefan's condition after the removal of nodes remains accurate.

6. CONCLUSION

The method developed in this paper is suitable for solving the axisymmetric Stefan problem. The method seeks a rapid solution to within machine accuracy by means of the Newton iteration. The method is also efficient because it incorporates adaptivity in space tessellation and automatic time step adjustments in time integration. Adaptivity of the spatial tessellation saves a lot of computation time if steep gradients are present, because only a small number of adaptive elements is needed to resolve the gradients. The time step adjustment also saves computation time because it avoids employing costly small time steps in a situation where a large time step is sufficient.

The second-order time-stepping procedure needs fewer time steps and fewer elements to complete the freezing computation with higher accuracy than the first-order time-stepping procedure. However, the first-order time-stepping procedure is simple and it is good enough for solving the freezing problem for most engineering purposes, where an accuracy to within 1–2% is acceptable.

The dynamics of the propagation of the freezing front in the freezing process when *Bi* is infinite are different from those in the freezing process when *Bi* is finite. In a freezing process with infinite *Bi*, the front starts advancing into the liquid with infinite speed. Whereas in a freezing process with finite *Bi*, the front starts advancing into the liquid with vanishing front speed.

Early node removal in the liquid domain might save some computation time. However, the front speed oscillates if the nodes are removed too early. It might even increase the computation time.

An extension of this method to two- and three-dimensional problems is not straightforward; we should find a suitable and handy method to tessellate the appearing and disappearing phases in two- and three-dimension adaptively. Some investigators [23, 24] have solved a two-dimensional transient Stefan's problem with constant temperature at the outer surface using moving and deforming elements. However, the same problem with convection or radiation at the outer surface remains an open problem.

Acknowledgements—The authors wish to thank the Minnesota Supercomputer Institute who provided grants for the computation time.

REFERENCES

1. J. Comini, S. Del Guidice, R. W. Lewis and D. C. Zienkiewicz, Finite element solution of non-linear heat conduction problem with special reference to phase change, *Int. J. Num. Meth. Eng.* **8,** 613–624 (1974).
2. R. Bonnerot and J. Jamet, A conservative finite element method for one-dimensional Stefan problems with appearing and disappearing phases, *J. Comp. Phys.* **41,** 357–388 (1981).
3. Y. Talmon, H. T. Davis and L. E. Scriven, Progressive freezing of composites analyzed by isotherm migration methods, *A.I.Ch.E. Jl* **27,** 928–937 (1981).
4. V. Voller and M. Cross, Accurate solution of moving boundary problems using the enthalpy method, *Int. J. Heat Mass Transfer* **24,** 545–556 (1981).
5. D. R. Lynch and K. O'Neill, Continuously deforming finite elements for the solution of parabolic problems, with and without phase change, *Int. J. Num. Meth. Eng.* **17,** 81–96 (1981).
6. H. M. Ettouney and R. A. Brown, Finite element methods for steady solidification problems, *J. Comp. Phys.* **49,** 118–150 (1983).
7. J. Crank, *Free and Moving Boundary Problems.* Clarendon Press, Oxford (1984).
8. K. Miller and R. N. Miller, Moving finite elements. I, *SIAM J. Numer. Anal.* **18,** 1019–1032 (1981).
9. R. E. Benner, Jr, H. T. Davis and L. E. Scriven, An adaptive finite element method for steady and transient problem, *SIAM J. Sci. Stat. Comput.* **8,** 529–549 (1987).
10. B. J. Pangrle, K. G. Ayappa, E. Sutanto, H. T. Davis, E. A. Davis and J. Gordon, Microwave thawing of lossy dielectric materials, University of Minnesota Supercomputer Institute Research Report UMSI 90/158 (1990).

11. H. S. Carslaw and J. C. Jaeger, *Conduction of Heat in Solids*, Chapter XI. Clarendon Press, Oxford (1959).
12. H. Budhia and F. Kreith, Heat transfer with melting or freezing in a wedge, *Int. J. Heat Mass Transfer* **16,** 195–211 (1973).
13. K. O'Neill, Fixed-mesh finite element solution for Cartesian two-dimensional phase change, *Trans. ASME* **105,** 436–441 (1983).
14. D. R. Lynch and J. M. Sullivan, Heat conservation in deforming element phase change simulation, *J. Comp. Phys.* **57,** 303–317 (1985).
15. D. R. Lynch and W. G. Gray, Finite element simulation of flow in deforming regions, *J. Comp. Phys.* **36,** 135–153 (1980).
16. J. F. Thompson, Z. U. A. Warsi and C. W. Mastin, *Numerical Grid Generation: Foundation and Applications*, Chapter V. Elsevier Science Publishing, Amsterdam (1985).
17. S. Adjerid and J. E. Flaherty, A moving finite element method with error estimation and refinement for one-dimensional time dependent partial differential equations, *SIAM J. Numer. Anal.* **23,** 778–796 (1986).
18. G. Strang and G. J. Fix, *An Analysis of the Finite Element Method*, pp. 53–63. Prentice-Hall, Englewood Cliffs, NJ (1973).
19. B. Noble and J. W. Daniel, *Applied Linear Algebra*, pp. 28. Prentice-Hall, Englewood Cliffs, NJ (1977).
20. P. M. Gresho, R. L. Lee and R. L. Sani, On the time-dependent solution of the incompressible Navier–Stokes equations in two and three dimensions. In *Recent Advances in Numerical Methods in Fluids* (Edited by C. Taylor and K. Morgan), Vol. 1, pp. 27–81. Pineridge Press, Swansea (1979).
21. G. Dahlquist and A. Björk, *Numerical Methods*, Chapter 8. (Translated by Ned Anderson.) Prentice-Hall, Englewood Cliffs, N.J. (1974).
22. E. Sutanto, H. T. Davis and L. E. Scriven, Liquid distributions in porous rock examined by cryo-scanning electron microscopy, SPE Paper 20518 (1990).
23. D. R. Lynch, Unified approach to simulation on deforming elements with application to phase change problems, *J. Comp. Phys.* **47,** 387–411 (1982).
24. M. R. Albert and K. O'Neill, Moving boundary–moving mesh analysis of phase change using finite elements with transfinite mappings, *Int. J. Num. Meth. Eng.* **23,** 591–607 (1986).